Research Article | Vol. 28, No. 13 / 22 June 2020 / Optics Express 19783
Optics EXPRESS

Performance studies of new optics for the time-of-flight detector of the AFP project

LIBOR NOZKA,[1,*] ANDREW BRANDT,[2] KAREL CERNY,[1] MIROSLAV HRABOVSKY,[1] TOMAS KOMAREK,[1] FILIP KRIZEK,[3] DUSAN MANDAT,[4] MARKO MILOVANOVIC,[5] MICHAEL RIJSSENBEEK,[6] PETR SCHOVANEK,[4] TOMAS SYKORA,[7] VLADIMIR URBASEK,[4] AND JAROMIR ZATLOUKAL[4]

[1]*Regional Centre of Advanced Technologies and Materials, Joint Laboratory of Optics of Palacky University and Institute of Physics AS CR, Faculty of Science, Palacky University, 17. listopadu 12, 771 46 Olomouc, Czech Republic*
[2]*The University of Texas at Arlington, Department of Physics, Box 19059, Arlington, TX 76019, USA*
[3]*Nuclear Physics Institute of the Czech Academy of Sciences, Husinec - Rez 130, 250 68 Rez, Czech Republic*
[4]*Institute of Physics of the Academy of Sciences of the Czech Republic, Na Slovance 2, Prague, Czech Republic*
[5]*DESY, Platanenallee 6 D-15738 Zeuthen, Germany*
[6]*Stony Brook University, Dept. of Physics and Astronomy, Nicolls Road, Stony Brook, NY 11794-3800, USA*
[7]*Charles University, Faculty of Mathematics and Physics, Institute of Particle and Nuclear Physics, V Holesovickach 2, CZ - 18000 Praha 8, Czech Republic*
[*]*libor.nozka@upol.cz*

Abstract: We present the results of performance studies of the upgraded optical part of the time-of-flight subdetector prototype for the AFP (ATLAS Forward Proton) detector obtained during the test campaign in a synchrotron test-beam facility with 5 GeV electrons at the DESY laboratory (Hamburg, Germany) in June 2019. The detection of the particle arrival time is based on generation of Cherenkov light in an L-shaped fused silica bar. In the previous version of the ToF, all bars were made of two pieces (radiator and light guide) glued together with a dedicated glue (Epotek 305). This solution suffers from additional radiation damage of glue. We adopted a new technique of bar production without the need of glue. The new bars have a higher optical throughput by a factor of 1.6, reduced fragility, and better geometrical precision.

1. Introduction

The design and the physics motivation for the need of time-of-flight (ToF) subdetector of the AFP project itself was already described thoroughly in our previous papers: the physics concept in [1,2], simulation benchmark studies [3], details of the optics in [4], and timing studies in [4,5]. The detection of the particle arrival time is based on generation of Cherenkov light in an L-shaped fused silica bar. For clarity, the geometry of the ToF detector is depicted in Fig. 1 together with its detailed view. The ToF assemblage consists of a 4×4 matrix of L-shaped bars made of fused silica (SK-1300 by O'Hara). Each bar serves both as a Cherenkov radiator and a light guide towards a fast multichannel-plate photomultiplier (MCP-PMT) device (the sensor plane in Fig. 1). The rows of four bars along the beam direction are called trains and are labeled with a number. The bars in each train are labeled with letters A, B, C, and D along the direction of the incoming particles. In this way, the bars in the Train 1 are labeled 1A, 1B, 1C, and 1D and so on for the other trains.

The L-shape design largely relies on a direct fast light propagation to the sensor (approximately 60% of all photon tracks in a bar accepted by the sensor). This means a bar has to be rotated

#394582 https://doi.org/10.1364/OE.394582
Journal © 2020 Received 8 Apr 2020; revised 12 Jun 2020; accepted 14 Jun 2020; published 19 Jun 2020

Optics EXPRESS

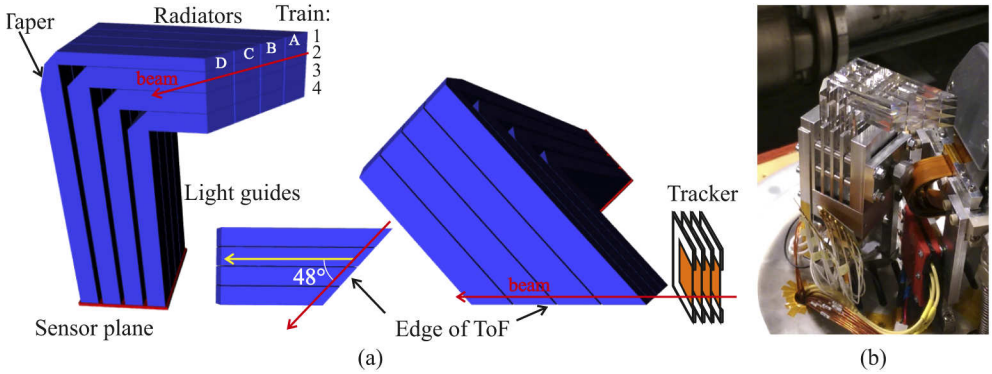

Fig. 1. (a) Geometry of the ToF subdetector, (b) a detailed view of installed ToF bars (reprint from [5]).

so that its radiator is tilted by the Cherenkov angle of 48 degrees with respect to the beam axis, Fig. 1(a). In addition, direct pathways need to be reflected on the bar elbow which means a 45 degrees cut coated with an appropriate reflection layer. The part of the light propagated using total reflections is delayed with respect to the fast direct propagation. The aforementioned studies [3] proposed a so-called taper to speed-up total-reflection pathways. On the other hand, adding a taper results in a correspondingly thinner radiator of a lower acceptance, see Fig. 1(a), Train 1. Moreover, a radiator cut is another design improvement allowing higher signal due to the additional back reflection of light with details described in [3]. Geometry of each bar is designed so that the cut planes of all bar radiators form an edge plane of the ToF detector, Fig. 1(a). Dimensions of the bars used in presented studies are summarized in Table 1 at the end of this section. Dimensions of all bars can be found in [4]. The passage length of beam particles through a radiator is 8.1 mm given by its thickness (6 mm) and tilt (48 degrees) with respect to the beam axis. The acceptance area of the AFP detector is 16.8×20.0 mm^2, given by dimensions of a tracker module in front [6] and its tilt as illustrated in Fig. 1(a).

Table 1. Dimensions of bars in Train 2. The bar elbow with the 45 degrees cut is part of the radiator.

	Radiator			Light guide		
Bar	Height [mm]	Thickness [mm]	Length [mm]	Width [mm]	Thickness [mm]	Length [mm]
2A	5	6	59.2	5	6	65.2
2B	5	6	53.5	5	6	65.2
2C	5	6	47.9	5	6	65.2
2D	5	6	42.3	5	6	65.2

The ToF detector was installed as a part of the AFP detectors in the forward region of the ATLAS detector on the Large Hardon Collider (LHC) in March of 2017. It was inserted into a movable Roman Pot together with the tracker [7] at about 220 m on both sides downstream the two beamlines. The working position was 1.5 mm from the beam centre. It ran till the end of 2017 in the LHC environment. The optics (and to a lesser extent the electronics) of the detector was exposed to high radiation at the level of 700 kGy at a distance of 5 mm from the beam centre. The bars themselves occupied a space in the region from 1.5 mm to 74.8 mm from the beam axis. There is a large gradient in the radiation level about 15 kGy/mm [7], as well as a specific shape of the illumination of the detector. This resulted in the development of activated hot spots in the bars as measured after their removal from the LHC tunnel.

Optics EXPRESS

We had tested the radiation hardness of the used fused silica glass SK-1300 and the glue Epotek 305 by means of a proton beam (30 MeV) generated in the cyclotron facility in Nuclear Physics Institute of the Czech Academy of Sciences in Rez near Prague (Czech Republic) [8]. We used circular samples (with outer diameter of 20 mm, and 2 mm thickness), some of them glued together with the Epotek 305 for the glue tests. The radiation effects were measured as a decrease of transmittance of the samples due to degradation of fused silica and of glue. The spectral region was in the interval from 115 nm to 350 nm set by the vacuum spectrometer used (the region of our interest was from 200 to 400 nm [3]). Figure 2(a) summarizes results relevant for this work. We applied radiation doses according to predicted levels in the LHC [3] (the *neq* stands for a neutron equivalent dose of the energy of 1 MeV): 700 kGy ($neq = 3 \cdot 10^{15} cm^{-2}$) for pure glass samples, 20 kGy ($neq = 9 \cdot 10^{13} cm^{-2}$) for the samples with the glue (the glue junction was at least 50 mm far from the beam center in the installation in the LHC).

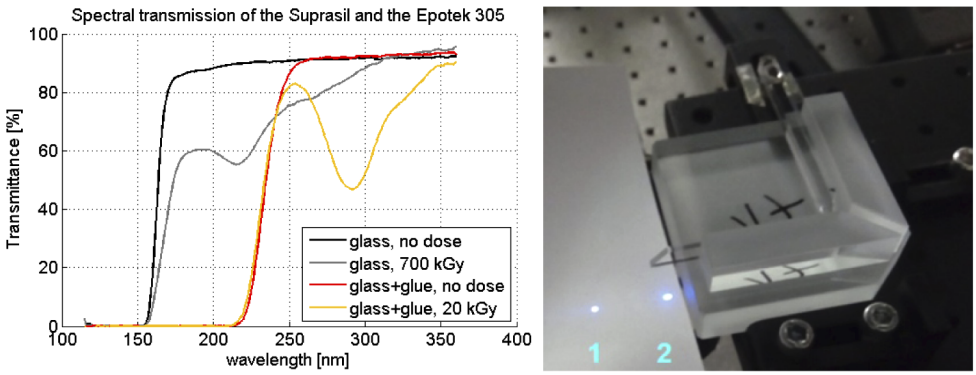

(a) (b)

Fig. 2. (a) Transmission spectra of the SK-1300 and Epotek 305 before and after radiation (including Fresnell losses), (b) splitting of a laser beam observed during transmittance measurements of irradiated bars.

The glass material of the bars was found to be sufficiently radiation hard. The transmittance of the glass stays above 50% within the wavelength range of 200–400 nm up to 700 kGy of irradiation dose. A significant decrease of transmittance due to irradiation occurs for wavelengths below 200 nm where the quantum efficiency of the photomultipliers is unknown but is expected not to be negligible. The glue itself deteriorates due to radiation in the order of tens of kGy and exhibits a transmittance drop around a wavelength of 292 nm, see Fig. 2(a). Thus, even while the bar material is sufficiently radiation hard, the glue reduces the radiation hardness of the full bars. This resulted in a steady decrease of their optical throughput during the operation in the LHC.

We measured the total decrease of transmittance of one of the irradiated bars (with the label 1D) after the operation in the LHC. The transmittance was measured by means of a laser beam of 280 nm wavelength (accidentally close to the transmittance drop of the glue). The measurement aimed to compare the signal power of the light beam passing the irradiated bar with one of non-irradiated bars of the same geometry. The observed decrease of transmittance was 38% ± 2% due to radiation at that wavelength. Moreover, during the measurement we noticed that the laser beam split at the glue layer as seen in Fig. 2(b). In the figure, the ordinary (expected) beam spot is labeled 2 and the parasitic spot is labelled 1. The intensity of the parasitic light beam was 40% of the signal level of the ordinary light beam.

The deterioration of the optical performance of the ToF detector due to permanent radiation damage contributed to the decline of its efficiency during operation. The efficiency is directly proportional to the average signal-to-noise ratio of the detector which in turn depends on the gain

Optics EXPRESS

of the photomultiplier. The gain is determined by the high voltage applied. However, the gain of photomultipliers for a constant high voltage decreases with higher rates of incoming light pulses [9,10]. This is critical for applications at the LHC which operates at the frequency of 40 MHz.

The development of L-shaped bars without a need of glue junction was highly desirable to improve the ToF timing performance and efficiency (including radiation hardness). The production of solid one-piece L-shaped bars was not trivial. The technique was chosen such that the skeleton of the whole train (four bars) was produced in one step considering a designed spacing of 0.4 mm between the bars in the installation. This allowed for precise alignment of adjacent surfaces of the bars, mainly at the edge of the ToF, see Fig. 1(a). Thus, the misalignment of the radiator arms (which was present in the case of glued L-bars) was removed. Then bars were polished individually. Train no. 2 of four solid (glueless) bars was produced for the June 2019 measurements at DESY in Hamburg. Their dimensions are summarized in Table 1.

In the following sections, we present results of the comparative measurement of the previously designed bars with the glue junction. Simulations were done to estimate the increase of number of photoelectrons compared to glued bars. We also needed to understand possible differences due to electron beam at the DESY test beam facility compared to the SPS (the Super Proton Synchrontron) beam at CERN we had used previously [5] (the SPS facility was closed during 2019). These studies are presented first.

2. Preparatory simulation studies

We focused on two tasks: (1) to perform studies of the effect of secondaries produced in the bars by the primary electron beam with energy of 5 GeV, (2) to assess the yield of photoelectrons given by solid bars compared to that of glued bars. The effect of secondaries is negligible in the case of the SPS beam at CERN (π^+ 120 GeV) as well as of the LHC beam (from this point of view the measurements with the SPS beam suited our needs better). Simulations of primary beam interactions with the whole Train 2 model were performed in the Geant4 framework [11]. The model contained the geometry of bars (Table 1), a model of the photomultiplier with its quantum efficiency [3] and a model of the stainless-steel entry window of the Roman pot which is 300 μm thick [7]. The beam goes into the Roman pot through this window. It is a thinned part of the Roman pot body. In the simulation, the photodetection efficiency (PDE) of the photomultiplier model was extrapolated down to 160 nm as a constant function of the wavelength with the value of 16% taken from the lowest known value at the wavelength of 200 nm.

Geant4 simulated the production of secondary electrons, positrons, and gamma photons induced by the primary electrons of the DESY beam passing the bars of the ToF detector. The gamma particles then partly convert to other electron-positron pairs. The electrons and positrons with kinetic energy above the threshold of 0.160 MeV generate additional Cherenkov photons. A negligible number of secondary positrons is generated in the case of the SPS beam. In total, according to the simulation, the DESY beam generates more secondary particles by a factor of 2.25 in the ToF detector than the SPS beam (only those secondary particles producing Cherenkov photons are counted here).

In the case showers are induced by the primary particles, the amount of secondary particles increases as the shower develops. As a result, the number of photoelectrons steadily increases from bar 2A to bar 2D. The comparison of the number of photoelectrons generated in the solid and glued bars 2A and 2D in full train is shown in Fig. 3 for the case of incident electron beam. Histograms were generated for 1000 events. In the case of bar 2A, the primary particles (the beam particles) generated 33 ± 6 photoelectrons, and secondary particles contributed with 7^{+10}_{-7} photoelectrons (there are large fluctuations). The total number of photoelectrons was 36 ± 9 (the filled histogram). In the case of bar 2D, we found 37 ± 6 photoelectrons by primary particles, and 23^{+30}_{-23} by secondaries, and 47 ± 21 photoelectrons in total. The number of photoelectrons given by secondary particles fluctuates strongly. This is due to relatively long interaction length of

Optics EXPRESS

relativistic electrons in fused silica for production of secondary gammas, electrons, and positrons (excluding Cherenkov photons) where the secondary electrons and positrons are generated by the conversion of secondary bremsstrahlung gammas.

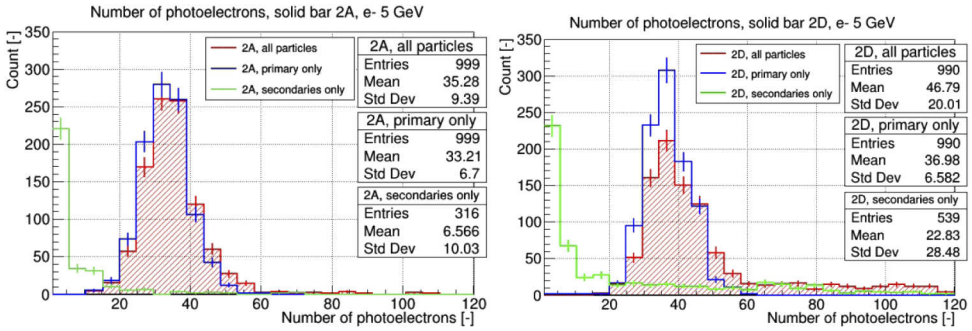

(a) (b)

Fig. 3. Simulated distribution of photoelectrons generated in the pixel of (a) the solid bar 2A, (b) the solid bar 2D for the 5 GeV e^- beam. Histograms were generated for 1000 events and full train installation.

In the case of the SPS beam, the influence of secondary particles is partly suppressed as the interaction length of relativistic pions in fused silica is even longer than for DESY electrons. Furthermore, the production of bremsstrahlung gammas is negligible compared to electron beams, and pions at 120 GeV have zero bremsstrahlung. Quantitatively, in the case of the bar 2A, the primary particles generated 34 ± 6 photoelectrons, secondary particles contribute with 5^{+6}_{-5} photoelectrons. The total number of photoelectrons is 35 ± 8. This is the same as for the bar 2A in the DESY beam. In the case of the bar 2D, we found 38 ± 6 photoelectrons by primary particles, 6^{+9}_{-6} by secondaries, and 40 ± 9 photoelectrons in total. Thus, the contribution by secondaries is almost the same across the whole train.

Concerning the yield of photoelectrons given by solid bars with respect to that of glued bars, we took the simulation with the DESY beam including contribution of secondaries. In this study we accounted for the spectral cut of the glue, see Fig. 2(a) (red curve). The result of this comparison study is shown in Fig. 4. It presents the simulated distributions of the total

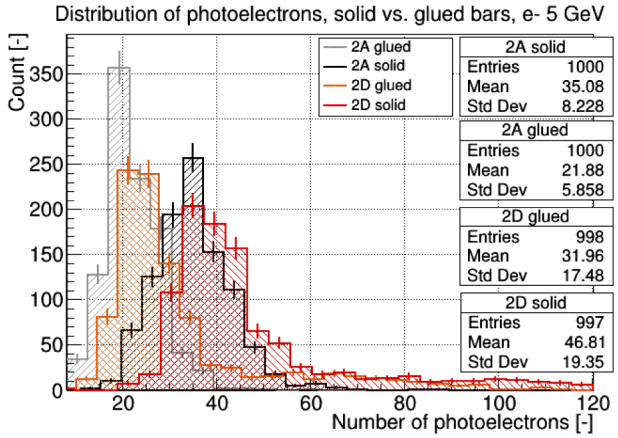

Fig. 4. Distributions of number of photoelectrons of selected solid and glued bars for the 5 GeV e^- beam. Histograms were generated for 1000 events and full train installation.

Optics EXPRESS

number of photoelectrons generated in the pixels occupied by the bars 2A and 2D in the full train scenario. Comparing the mean values relevant to all particles, we can derive an improvement in the number of photoelectrons. The bar 2A improved by a factor of 1.6. This stands for all single bars including a single 2D bar (we did comparisons for all single bars, we excluded corresponding histograms for brevity). In the case of bar 2D in the full train installation, the improvement factor dropped to 1.5 (partly due to a relatively smaller increase of contribution by secondaries by a factor of 1.3, and partly due to a higher attenuation of those deep UV photons coming from upstream bars).

Note that the presented ToF model lacks a model of the photomultiplier response. In reality, there is an extra electronic crosstalk between pixels which additionally strengthen the signal in each of them in the case of full train installation [5].

3. Experimental setup

The experimental measurements were done on the T22 beamline of the DESY II synchrotron [12] in the last week of June 2019. The synchrotron facility provided an electron beam which was set to an energy of 5 GeV. The experimental setup was similar to the one used in previous measurements [4,5]. The only change was to use the Roman pot instead of the auxiliary duralumin dark box. The scheme of the measurement setup is shown in Fig. 5 together with a picture.

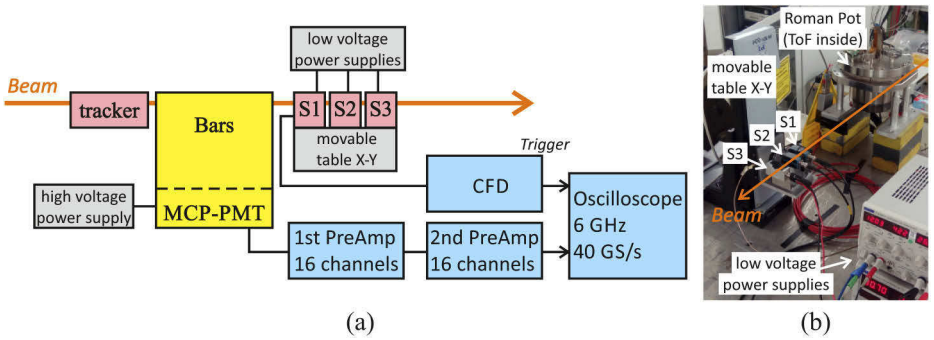

Fig. 5. (a) Scheme of the experimental setup, (b) picture of the installation in DESY.

We used the MCP photomultiplier Photonis XPM85112/A1-S (SN 9002091) with 4×4 pixelization, and a sapphire entrance window, and a reduced anode gap. Its MCP (multichannel plate) resistance was 16 MΩ, a gain of 10^5 at an overall high voltage of 2190 V, and a gain 10^6 at 2525 V. Train 2 with the full complement of 4 bars (solid or glued) was installed on top of the photomultiplier aligned to its pixelization [5]. The output signal from each pixel (channel) was amplified by two stages of voltage preamplifiers (each with a gain of 10) and collected by means of a fast LeCroy WaveMaster 806Zi-B oscilloscope (bandwidth 6 GHz, sampling 40 GS/s). The oscilloscope was triggered by the signal from one of three detectors S1, S2, and S3 downstream of the beam. Each trigger detector consisted of a 15 mm long fused silica bar of 3×3 mm^2 cross-section coupled to a silicon photomultiplier (SiPM) manufactured by ST Microelectronics (S1, S2, type: NRD09_1 with 3.5×3.5 mm^2 and 58 μm cell size) [13] or by SensL (S3) [14] that detected Cherenkov radiation. They were placed on a two-axis movable stage (remotely controlled) to select a specific area of the ToF detector for study. We mostly used the first detector S1 (the closest to the ToF) as a trigger. The others were used for the measurement of their mutual resolution and, in turn, the resolution of the S1. The signal from the S1 detector was preprocessed by a CFD unit (Constant Fraction Discriminator) to minimize its time-walk (with a threshold value of -400 mV).

Optics EXPRESS

4. Measurements and results

During all measurements, we positioned the trigger to have its coincidence with the following ToF areas in the beam: 0 mm from the edge (the edge position, see Fig. 1(a)), 5 mm, and 9 mm from the edge. First, we measured the timing resolution of the trigger (S1) by means of a comparative timing resolution measurement among all SiPM detectors. The timing resolution of the trigger S1 detector was found to be 13 ± 1 ps. Then we measured single bars and the whole train of the glued and the solid bars for different gains of the photomultiplier. The gain was set by varying levels of the applied high voltage.

4.1. Signal strength

Figure 6 shows the signal strength (amplitude) of single bars for both the solid (the rich colors) and the glued (the pale colors) versions measured at a distance of 5 mm from the edge of the bars. The bars were measured at high voltages of 2050 V, 2100 V, 2150 V, and 2200 V. The signal strength of the glued bars at 2050 V was poor and is not plotted. Similarly, solid bars produced too saturating signal pulses at 2200 V, so we decided to omit this measurement. Each distribution is described by a box defining the interval from the 25% (Q1) to 75% (Q2) quantiles of the amplitude distribution with a level mark inside indicating the median value (50% quantile). The dashed line with endings defines the interval from the minimum value to the maximum value of the distribution excluding outliers (red points in the tail). The lower outliers are the values lower than Q1-1.5*(Q2-Q1). The results exhibit large fluctuations which is a characteristic for the ToF detector and due to low level of the input Cherenkov signal [4]. Concerning the median values, we required an optimum level of -300 mV for a good separation of the signal from the pedestal for the given amplification. The pedestal was a white noise produced by a PMT anode resistor (50 Ω), dark counts of the PMT, and both preamplifier stages. The pedestal cut itself was -150 mV. Similar results from measurements at the edge and at a distance of 9 mm from the edge are not presented here for the sake of brevity but they are mentioned in text.

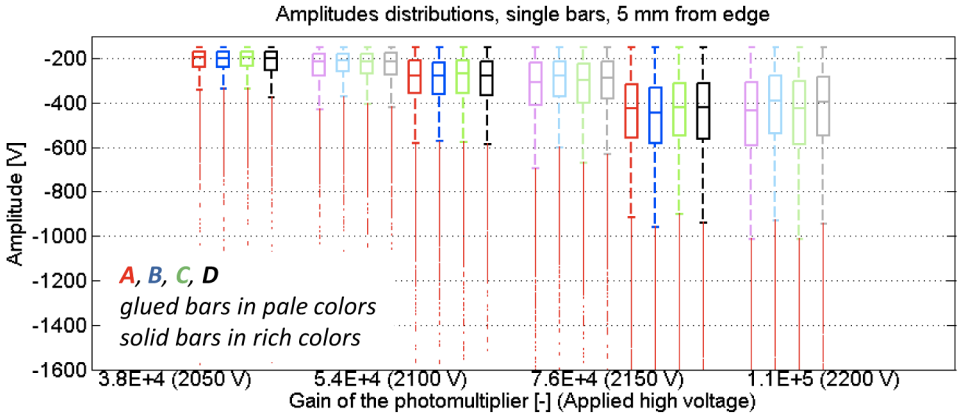

Fig. 6. Signal strength of single bars measured at a distance of 5 mm from the edge of the ToF for various gains of the photomultiplier.

At the distance of 5 mm from the edge, the setup with solid bars reached the optimum level at a gain of $7.6 \cdot 10^4$ (corresponding HV=2150 V) and the one with glued bars at a gain of $1.1 \cdot 10^5$ (2200 V). At the edge, the values of the gain were $5.4 \cdot 10^4$ (2100 V) and $7.6 \cdot 10^4$ (2150 V) for the solid bars and glued bars respectively. As for the 9 mm case, the optimal gain values were almost the same as for the case of 5 mm from the ToF edge. The main conclusion of these results

Optics EXPRESS

is that single solid bars produced a signal higher by a factor of 1.6–1.8 compared to the glued bars for the same PMT gain. Further interpretation is done in the Discussion section below.

The situation changed with the bars installed in the full train as seen in Fig. 7. Due to light leakage from the upstream bars, the downstream bars profit from the photon enrichment and consequently register higher number of photons by a factor up to 1.4 [4]. Besides, any secondaries produced further increase the signal level of downstream bars as mentioned earlier. As a result, the light in the downstream bars is always augmented. The first bar (A) is the only one having a signal strength the same as in the single bar scenario (excluding the effect of the electronic crosstalk from the adjacent bar 2B). Note a weaker signal amplitude of the 2D bar compared to the one of the 2C bar. We presume this is due to lower signal contribution from adjacent pixels (charge sharing between pixels) - the 2D-bar pixel has only one adjacent pixel within the train. However, this effect was not studied in more detail (the leakage effect between pixels was addressed in [5], Fig. 5).

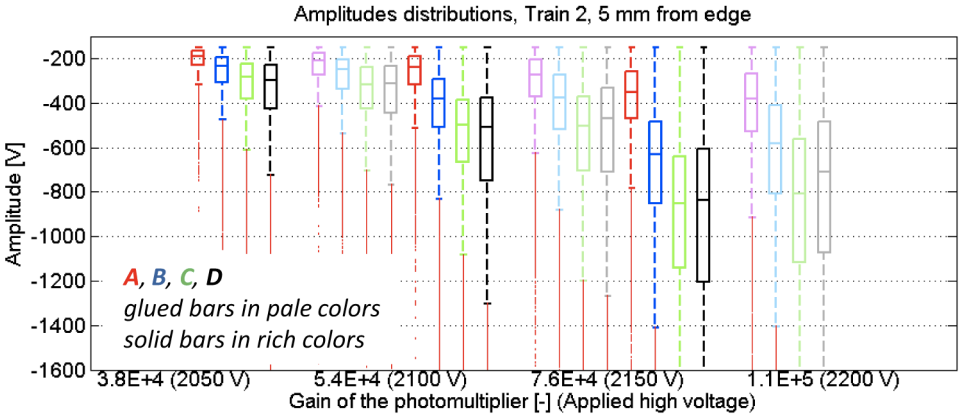

Fig. 7. Signal strength of bars installed in the train measured at a distance of 5 mm from the edge of the ToF for various gains of the photomultiplier.

The signal strength of the train is closely related to the efficiency of the train which is an important performance characteristic. We directly measured the efficiency with respect to the SiPM trigger during the measurement campaign. We evaluated the train efficiency for the cases (called majority trigger cases) in which either all four bars ('=4'), at least three bars ('>=3'), at least two bars ('>=2'), or at least one bar ('>=1') generated a valid signal with the amplitude larger than the signal-to-pedestal threshold of -150 mV. The '=4' case and the '>=3' case were of the main interest (due to better train resolution, see below). The results are summarized in Table 2. The values obtained at the preferred gains are highlighted. The efficiency of the '=4' case is affected by a lower signal strength of the bar 2A with respect to other bars in the train (there is no enrichment by photons from upstream bars). As the signal level of the solid bar 2A is much higher (by a factor of 1.6, as seen above), the solid train has significantly higher efficiency as compared to its glued counterpart for the '=4' case. See the Discussion section below for further discussion of this result.

4.2. Timing resolution

Concerning the timing resolution, we measured the resolution of single bars and that of full trains. The measurements of the timing resolution of the bars and the whole trains were performed with respect to the first SiPM detector acting as a trigger. We preprocessed the output signal by the CFD module. The timestamp of leading edge was treated as the arrival time of a signal pulse. The arrival time of a signal pulse from a PMT pixel was determined relative to the arrival time of

Optics EXPRESS

Table 2. Efficiency of the ToF measured with respect to the SiPM trigger for the amplitude threshold of -150 mV at the distance of 5 mm from the edge.

		Glued bars				Solid bars			
		Number of bars with detectable signal				Number of bars with detectable signal			
HV [V]	Gain [-]	=4	>=3	>=2	>=1	=4	>=3	>=2	>=1
2050	$3.8 \cdot 10^4$	-	-	-	-	20%	68%	90%	94%
2100	$5.4 \cdot 10^4$	28%	68%	89%	94%	**67%**	**91%**	**93%**	**95%**
2150	$7.6 \cdot 10^4$	**66%**	**90%**	**93%**	**95%**	89%	93%	94%	95%
2200	$1.1 \cdot 10^5$	86%	93%	94%	96%	-	-	-	-

the trigger (the time difference). In the following, we express the timing resolution by the sigma parameter of the Gaussian fit of the timestamp distributions [5].

Results are summarized in Table 3 (with uncertainty of ±2 ps) for single bars at the distance of 5 mm from the edge. Here, the values of measured timing resolutions stand for the bars after subtraction of the trigger contribution of 13 ± 1 ps. The values obtained for the proposed gains are highlighted. Data were filtered out with the signal amplitude larger than the threshold -150 mV. Note that the timing resolution of the photomultiplier pixels varies, and this variation notably contributes to the results. Concerning the other distances from the edge, the timing resolutions at the edge were better by 5 ± 2 ps on average and the ones at the 9 mm distance from the edge were slightly better by 1 ps on average with respect to the 5 mm distance case.

Table 3. Timing resolution of single bars in [ps] (uncertainty ±2 ps) for the amplitude threshold of -150 mV at a distance of 5 mm from the edge.

Bar	Glued bars			Solid bars		
	Gain $5.4 \cdot 10^4$ (HV 2100 V)	Gain $7.6 \cdot 10^4$ (HV 2150 V)	Gain $1.1 \cdot 10^5$ (HV 2200 V)	Gain $3.8 \cdot 10^4$ (HV 2050 V)	Gain $5.4 \cdot 10^4$ (HV 2100 V)	Gain $7.6 \cdot 10^4$ (HV 2150 V)
2A	40	**39**	35	49	**46**	42
2B	40	**38**	36	47	**43**	40
2C	39	**36**	32	45	**43**	40
2D	38	**36**	34	44	**41**	38

For the same gain of the photomultiplier, the solid bars gave worse resolution by 3 ± 2 ps on average (for all scanned distances from the edge). However, the difference grew to 6 ± 2 ps comparing the timing resolutions for the optimal gains, i.e. $7.6 \cdot 10^4$ for glued bars and $5.4 \cdot 10^4$ for solid bars. This additional worsening of the timing resolution was due to lower gain of the photomultiplier in the case of the solid bars. Nevertheless, the worse resolution of the solid bars for the same gain was a surprising finding in the light of the significant improvement in the light throughput resulting in a higher number of photoelectrons in the photomultiplier.

The timing resolution of the whole Train 2 was measured with all bars of the train installed on the photomultiplier. It was calculated from a distribution of arithmetic averages of timestamps given by individual bars in the train which produced a valid signal (they were triggering). For the case of all four bars triggered ('=4'), the train resolution is theoretically expected to be ½ of the timing resolution of a single bar in the train provided all four bars have the same resolution and no correlation exists between them. In practice, however, the correlation of timestamps among the bars is non-negligible due to electronic crosstalk (the optical crosstalk has no effect here as discussed in [5]). This results in a worsening of the timing resolution of the train. The timing resolution of a train depends on the number of triggering bars. Fewer triggering bars leads to a worse resolution. The timing resolutions given by our measurements are summarized in Table 4

Optics EXPRESS

(with uncertainty of ±2 ps) for all assumed majority trigger cases measured at the 5 mm distance of from the edge. The resolution contribution 13 ps from the SiPM trigger was subtracted. The highlighted values stand for the preferred gain levels of the PMT as were mentioned before.

Table 4. Timing resolution of Train 2 in [ps] (uncertainty ±2 ps) for different majority trigger cases (the amplitude threshold of -150 mV, at the distance of 5 mm from the edge).

Case	Glued bars			Solid bars		
	Gain $5.4 \cdot 10^4$ (HV 2100 V)	Gain $7.6 \cdot 10^4$ (HV 2150 V)	Gain $1.1 \cdot 10^5$ (HV 2200 V)	Gain $3.8 \cdot 10^4$ (HV 2050 V)	Gain $5.4 \cdot 10^4$ (HV 2100 V)	Gain $7.6 \cdot 10^4$ (HV 2150 V)
>=1	30	**28**	30	30	**28**	30
>=2	27	**28**	28	29	**28**	29
>=3	27	**27**	27	27	**28**	27
=4	26	**28**	28	27	**27**	28

At the first sight, the timing resolution of both trains were worse by about 10 ps with respect to the output from measurements on the SPS beam [4,5]. This issue is caused by the beam itself. Nevertheless, the timing resolution was the same for both the glued and the solid trains, regardless of the applied majority trigger. There is also no distinction between the majority trigger cases although the train resolution deteriorates with a lower number of triggering bars. This is due to high relative occurrence of cases with three and four bars involved in the arrival time measurement. This is indicated in Table 5 where results for individual number of triggering bars are plotted (exactly a one bar triggered etc.) together with their relative occurrence in the dataset. They are labeled as the 'equal' cases. At the first sight, the '=1' and '=2' cases are almost suppressed. Note the worse timing resolution values for the '=1' case with respect to the values for single bars in Table 3. This is assumed to be due to the electronic crosstalk from the other channels (even when they did not pass the trigger threshold) which affect the clarity of the signal (there is no electronic crosstalk in the single bar case). See the next section for further discussion of the results.

Table 5. Timing resolution of the Train 2 in [ps] for different 'equal' cases of triggering bars (the amplitude threshold of -150 mV, at the distance of 5 mm from the edge) together with their relative occurrence in measured data.

	Glued bars						Solid bars					
	Gain $5.4 \cdot 10^4$ (HV 2100 V)		Gain $7.6 \cdot 10^4$ (HV 2150 V)		Gain $1.1 \cdot 10^5$ (HV 2200 V)		Gain $3.8 \cdot 10^4$ (HV 2050 V)		Gain $5.4 \cdot 10^4$ (HV 2100 V)		Gain $7.6 \cdot 10^4$ (HV 2150 V)	
Case	σ [ps]	occ.	σ [ps]	occ.	σ [ps]	occ.	σ [ps]	occ.	σ [ps]	occ.	σ [ps]	occ.
=1	54 ± 5	5%	44 ± 5	2%	38 ± 5	2%	53 ± 5	4%	44 ± 5	1%	45 ± 5	1%
=2	30 ± 2	21%	29 ± 2	4%	27 ± 5	2%	32 ± 5	21%	27 ± 5	2%	41 ± 5	1%
=3	26 ± 2	41%	25 ± 2	24%	25 ± 2	7%	26 ± 2	48%	26 ± 2	24%	24 ± 5	4%
=4	26 ± 2	28%	28 ± 2	66%	28 ± 2	86%	27 ± 2	20%	27 ± 2	67%	28 ± 2	89%

5. Discussion

The main message from these measurements is the improvement by a factor of at least 1.6 of the signals produced with the single solid bars compared to their glued counterparts. This is in good agreement with simulations (Fig. 4, bar 2A) which predicted the wavelength cut of the glue at 235 nm removes more than one third of the useful Cherenkov light. However, the simulation underestimated the amplitude improvement of the 2D bar in the full train (a factor of 1.5 in simulation). We assume this is due to the fact our model does not comprise additional

Optics EXPRESS

interaction between bar channels at the photomultiplier level (namely charge sharing) and the response of the photomultiplier overall. In the simulation, the photodetection efficiency (PDE) of the photomultiplier model was extrapolated down to 160 nm as a constant function of the wavelength with the value of 16% taken from the lowest known value at the wavelength of 200 nm. The good agreement between data and the simulation proved that the PDE of the used photomultiplier is significant below 200 nm despite being unknown in the deep UV region.

For proper operation, a good separation of the signal from the pedestal is required. In the setup, a threshold of -150 mV was the optimum value. The required mean signal amplitude is then -300 mV or bigger. The corresponding optimum gain for the glued bars was $7.6 \cdot 10^4$, and $5.4 \cdot 10^4$ for the solid bars.

The rate of our beam test events at DESY (and at the SPS in the past) was of order of kHz, a rate that does not affect the performance of the photomultiplier. In such conditions, the efficiency of the ToF with the solid bars was substantially higher compared to the glued counterpart for the same gain, see Table 2. This is especially true for the '=4' trigger condition in which we require all bars in the train to produce a valid signal (surpassing the signal-to-pedestal threshold of -150 mV). However, if we reduce the gain from $7.6 \cdot 10^4$ to $5.4 \cdot 10^4$ for solid bars we end up with the same efficiency as for glued bars at a gain of $7.6 \cdot 10^4$ (keeping in mind we operate in a low-rate regime).

The timing resolution is the main performance characteristic of the ToF detector. Although the timing resolution of the train is the decisive parameter, we also focused on the timing performance of the single bars. According to the Table 3, the solid bars gave worse resolution by 3 ± 1 ps in average for the same gain. This was surprising. We expected a slightly better resolution due to higher number of photons on the photomultiplier photocathode despite the fact there is a saturation of the timing resolution of photomultipliers with the increasing number of photoelectrons as reported in [15]. We tried to explain this deterioration as the effect of the Cherenkov light dispersion. As the solid bars miss the glue layer, the wavelength range of accepted photons spreads down to 160 nm where the index of refraction of the fused silica (and of dielectrics in general) quickly rises. However, our simulation did not reveal any significant change of the time distribution of photons hit counts on the PMT photocathode. On the other hand, these distinctions disappeared when all bars were installed in the train and we studied the timing performance of the whole train. When a train average time is determined, the difference of 3 ps present in the timing resolution of single bars (solid vs. glued) is suppressed. Theoretically, the resolution of the train is half of the single bar resolution. Thus, the difference is 1.5 ps in case of the full train which is comparable with our uncertainty of measurement.

It is interesting that the train timing resolution did not change (within the uncertainty of ± 2 ps) among the applied majority triggers. Thus the '>=1' case gave the same timing performance as the '>=3' or '=4' cases. The explanation is found in Table 5. The relative occurrence of the '=1' case (exactly only one of bars triggered) or the '=2' case was below 5%. Actually, most frequently all four bars triggered (66% or 67%), followed by the case in which at least three bars were triggering (24%). The best timing resolution was obtained for the case '=3'. The '=4' case suffered somewhat from the poorer timing performance of the first bar as no photon enrichment is present from the upstream bars. Adding a fake bar in front of the first bar would solve this issue. However, there is lack of space for such modifications. From these results we can deduce which of the majority trigger cases to use for the ToF operation based on the timing resolution and the efficiency. The selection criterion based on the '>=3' case is optimal.

It is known that the real gain of MCP photomultipliers decreases for high rates of incoming light pulses [9,16]. This is related to a growth of the average charge collected on the photomultiplier's anode and the speed of its drainage. This effect plays a critical role in the deployment of the ToF detector in the LHC collider with the 40 MHz bunch crossing rates. The expected frequency of pulses is 20 MHz per train for the forthcoming pile-up mode of the collider. Figure 8 plots

Optics EXPRESS

rate characteristics of the used PMT for the gains of $5.4 \cdot 10^4$ and $7.6 \cdot 10^4$ and various output amplitudes at the low frequency of 10 kHz (the reference amplitudes). These measurements were performed on a picosecond laser at the wavelength of 402 nm, see [10] for details concerning the measurement setup. The whole PMT was uniformly illuminated and only the channel (pixel) 22 was measured (no Cherenkov bars were installed). Output signals were amplified with the same preamplifiers as used in the DESY beam tests. Measurements were performed in the range of 10 kHz to 50 MHz or less where the strip current exceeded the safe value of 500 μA (the black and purple curves, see below). For each scan, the relative amplitude was calculated as the ratio of the measured mean output amplitude to the one measured at 10 kHz, see Fig. 8(b). Note that the level of the noise does not depend on the pulse rates.

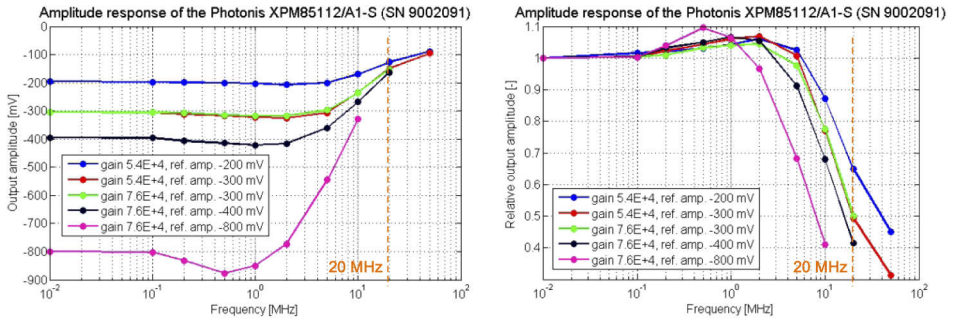

Fig. 8. Results of the rate scans of the PMT Photonis XPM85112/A1-S (a) in terms of measured output amplitudes, (b) in terms of relative amplitudes with respect to the one at 10 kHz (the lowest frequency).

In Fig. 8, the configuration with gain $5.4 \cdot 10^4$ and reference amplitude -200 mV (blue curve) corresponds to a single glued bar, at that gain, from the DESY test (Fig. 6). It provided the lowest attenuation at increased input rate, likely due to the lowest generated charge on the MCP-PMT. Similarly, the configuration with gain $5.4 \cdot 10^4$ and reference amplitude -300 mV (red curve) corresponds to a single solid bar from the same test. The configuration with gain $7.6 \cdot 10^4$ and reference amplitude -300 mV (green curve) corresponds to a single glued bar at that gain. Both red and green configurations had similar rate characteristics as they produced the same charge in the multi-channel plate.

The configuration with gain $7.6 \cdot 10^4$ and reference amplitude -400 mV (black curve) corresponds to a single solid bar at that gain. The last configuration with gain $7.6 \cdot 10^4$ and reference amplitude -800 mV (purple curve) corresponds to the full installed train, at that gain, from the DESY test (Fig. 7). The last case had the worst rate performance due to relatively high level of charge generated on the PMT anode.

At the rate of 20 MHz, all configurations (except the purple one) provide similar amplitudes of approximately -150 mV. This is related to the fact that there is a limited charge available in the PMT for the electron multiplication in its MCP plates. However, this amplitude is also the level of the pedestal separation in our ToF setup. In other words, the efficiency of detection using ToF with the photomultiplier as used is very low at the expected operating rate of 20 MHz. One can overcome this issue by decreasing of the PMT gain by for example the factor of 5 and add an extra amplification stage to compensate and get back to the optimal level for the CFD operation. But the timing resolution deteriorates due to worse signal-to-noise ratio. As indicated in [10], the timing resolution then gets worse by a factor of 2-3. Then, an additional noise level reduction is required.

Optics EXPRESS

6. Conclusion

We designed and tested new type of optical bars of the ToF detector for the AFP project. To obtain the required L-shape, the bars were previously made by gluing together two separately produced arms of the bar. This resulted in a degradation of their optical throughput. Recently a new production technique was developed allowing for a production of a glueless (solid) version of the bars. We successfully tested these during the June 2019 campaign at DESY in a 5 GeV electron beam. The results presented here confirmed our expectations concerning the strength of the signal produced by the ToF detector and its measurement efficiency. However, the timing resolution remained unchanged because of limitations on the photomultiplier side. Theoretically, there is still a room for further improvements on the optical system (a fake front bar or radiator). On the other hand, the photomultiplier is the most limiting element due to its behavior in the regime of high rates of incoming relativistic particles.

Funding

Ministerstvo Školství, Mládeže a Tělovýchovy (LM2015056, LM2018104); European Regional Development Fund (CZ.02.1.01/0.0/0.0/16_013/0001403, CZ.02.1.01/0.0/0.0/16_019/0000754, CZ.02.1.01/0.0/0.0/17_049/0008422); Univerzita Palackého v Olomouci (IGA_Prf_2020_007).

Acknowledgments

The measurements leading to these results have been performed at the Test Beam Facility at DESY Hamburg (Germany), a member of the Helmholtz Association (HGF).

Disclosures

The authors declare no conflicts of interest.

References

1. A. B. Kaidalov, V. A. Khoze, A. D. Martin, and M. G. Ryskin, "Extending the study of the higgs sector at the lhc by proton tagging," Eur. Phys. J. C **33**(2), 261–271 (2004).
2. FP420 Collaboration, "The FP420 R&D project: Higgs and New Physics with forward protons at the LHC," Nucl. Instrum. Methods Phys. Res., Sect. A **4**(10), T10001 (2009).
3. L. Nozka, A. Brandt, M. Rijssenbeek, T. Sykora, T. Hoffman, J. Griffiths, J. Steffens, P. Hamal, L. Chytka, and M. Hrabovsky, "Design of cherenkov bars for the optical part of the time-of-flight detector in geant4," Opt. Express **22**(23), 28984–28996 (2014).
4. L. Nozka, L. Adamczyk, G. Avoni, A. Brandt, P. Buglewicz, E. Cavallaro, G. Chiodini, L. Chytka, K. Ciesla, P. M. Davis, M. Dyndal, S. Grinstein, P. Hamal, M. Hrabovsky, K. Janas, K. Jirakova, M. Kocian, T. Komarek, K. Korcyl, J. Lange, D. Mandat, V. Michalek, I. L. Paz, D. Northacker, M. Rijssenbeek, L. Seabra, P. Schovanek, R. Staszewski, P. Swierska, and T. Sykora, "Construction of the optical part of a time-of-flight detector prototype for the AFP detector," Opt. Express **24**(24), 27951–27960 (2016).
5. L. Chytka, G. Avoni, A. Brandt, E. Cavallaro, P. M. Davis, F. Foerster, M. Hrabovsky, Y. Huang, K. Jirakova, M. Kocian, T. Komarek, K. Korcyl, J. Lange, V. Michalek, L. Nozka, I. L. Paz, M. Rijssenbeek, P. Schovanek, T. Sykora, and V. Urbasek, "Timing resolution studies of the optical part of the AFP time-of-flight detector," Opt. Express **26**(7), 8028–8039 (2018).
6. J. Lange, E. Cavallaro, S. Grinstein, and I. L. Paz, "3D silicon pixel detectors for the ATLAS Forward Physics experiment," Nucl. Instrum. Methods Phys. Res., Sect. A **10**(03), C03031 (2015).
7. L. Adamczyk, E. Banas, A. Brandt, M. Bruschi, S. Grinstein, J. Lange, M. Rijssenbeek, P. Sicho, R. Staszewski, T. Sykora, M. Trzebinski, J. Chwastowski, and K. Korcyl, "Technical Design Report for the ATLAS Forward Proton Detector," (2015) Technical Report CERN-LHCC-2015-009. ATLAS-TDR-024.
8. F. Krizek, J. Ferencei, T. Matlocha, J. Pospisil, P. Pribeli, V. Raskina, A. Isakov, J. Stursa, T. Vanat, and K. Vysoka, "Irradiation setup at the U-120M cyclotron facility," Nucl. Instrum. Methods Phys. Res., Sect. A **894**, 87–95 (2018).
9. A. Tremsin, J. Pearson, G. Fraser, W. Feller, and P. White, "Microchannel plate operation at high count rates: new results," Nucl. Instrum. Methods Phys. Res., Sect. A **379**(1), 139–151 (1996).
10. T. Komarek, A. Brandt, V. Chirayath, L. Chytka, M. Hrabovsky, L. Nozka, M. Rijssenbeek, T. Sykora, and V. Urbasek, "Timing resolution and rate capability of Photonis miniPlanacon XPM85212/A1-S MCP-PMT," *In review process* (2020).

Optics EXPRESS

11. Geant4 Collaboration, "Recent developments in Geant4," Nucl. Instrum. Methods Phys. Res., Sect. A **835**, 186–225 (2016).
12. R. Diener, J. Dreyling-Eschweiler, H. Ehrlichmann, I. M. Gregor, U. Kotz, U. Kramer, N. Meyners, N. Potylitsina-Kube, A. Schutz, P. Schutze, and M. Stanitzki, "The DESY II test beam facility," Nucl. Instrum. Methods Phys. Res., Sect. A **922**, 265–286 (2019).
13. M. Albrow, H. Kim, S. Los, M. Mazzillo, E. Ramberg, A. Ronzhin, V. Samoylenko, H. Wenzel, and A. Zatserklyaniy, "Quartz Cherenkov Counters for Fast Timing: QUARTIC," Nucl. Instrum. Methods Phys. Res., Sect. A **7**(10), P10027 (2012).
14. M. Bonesini, T. Cervi, A. Menegolli, M. C. Prata, G. L. Raselli, M. Rossella, M. N. Spanu, and M. Torti, "Detection of vacuum ultraviolet light by means of SiPM for high energy physics experiments," Nucl. Instrum. Methods Phys. Res., Sect. A **912**, 235–237 (2018).
15. J. Vavra, D. W. G. S. Leith, B. Ratcliff, E. Ramberg, M. Albrow, A. Ronzhin, C. Ertley, T. Natoli, E. May, and K. Byrum, "Beam test of a time-of-flight detector prototype," Nucl. Instrum. Methods Phys. Res., Sect. A **606**(3), 404–410 (2009).
16. F. Uhlig, A. Britting, W. Eyrich, A. Lehmann, C. Schwarz, and J. Schwiening, "Performance studies of microchannel plate pmts," Nucl. Instrum. Methods Phys. Res., Sect. A **695**, 68–70 (2012).